

Observation and spectroscopy of a two-electron Wigner molecule in an ultraclean carbon nanotube

S. Pecker^{*1}, F. Kuemmeth^{*2}, A. Secchi^{3,4†}, M. Rontani³, D. C. Ralph^{5,6}, P. L. McEuen^{5,6}
and S. Ilani¹

¹*Department of Condensed Matter Physics, Weizmann Institute of Science, Rehovot 76100, Israel*

²*Center for Quantum Devices, Niels Bohr Institute, University of Copenhagen, Universitetsparken 5, DK-2100 Copenhagen, Denmark*

³*CNR–NANO Research Center S3, Via Campi 213/a, 41125 Modena, Italy*

⁴*Department of Physics, University of Modena and Reggio Emilia, 41125 Modena, Italy*

⁵*Physics Department, Cornell University, Ithaca, New York 14853, USA*

⁶*Kavli Institute at Cornell, Cornell University, Ithaca, New York 14853, USA*

**These authors contributed equally to this work.*

†Present address: Institute for Molecules and Materials, Radboud University of Nijmegen, 6525 AJ Nijmegen, The Netherlands

- S1. Symmetries of two-electron states in carbon nanotubes**
- S2. Direct measurement of the single-particle level spacing**
- S3. Comparison of one-electron and two-electron addition spectra.**
- S4. Inter-valley Coulomb interactions in the observed addition spectrum**
- S5. Addition spectrum and detuning dependence of two holes in a single dot.**
- S6. The complete detuning dependence of excited-state spectra from positive and negative bias measurements.**
- S7. Exact diagonalization**

S1. Symmetries of two-electron states in carbon nanotubes

Electronic wavefunctions in carbon NTs consist of three components: a real-space component along the tube, a spin component, and an ‘isospin’ component related to the clockwise or counter-clockwise motion of the electron around the tube’s circumference[†]. Although the isospin is formally also a spatial degree of freedom, energetically it is well decoupled from the spatial component along the tube and is in fact strongly coupled to the spin degree of freedom via spin-orbit coupling. Thus, the total wavefunction is naturally decomposed into a spatial and a spin-isospin components: (*spatial*) \otimes (*isospin* \otimes *spin*). For a single electron, for each particle-in-a-box level in real space there are four possible spin-isospin combinations. Correspondingly, for two electrons there are $4 \times 4 = 16$ spin-isospin combinations. In this section we show how these states fall into multiplets with distinct symmetries and highlight which of these states should be visible in tunneling spectroscopy.

Since the total wavefunction of two electrons has to be anti-symmetric under exchange of electrons, the behavior in the spatial and the spin-isospin subspaces is anti-correlated: If the wave function is symmetric (S) in real space it must be anti-symmetric (-) in spin-isospin space. Similarly, if it is anti-symmetric (AS) in real space, it has to be symmetric (+) in spin-isospin space. Note that throughout the main text we refer to the $2e$ states through their symmetry in real space (S or AS), since this is the degree of freedom that naturally couples to Coulomb interactions.

The breakdown of the 16 two-electron spin-isospin combinations according to their symmetries is as follows: To form a ‘singlet-like’ (-) state in spin-isospin subspace we can combine a singlet in spin with a triplet in isospin and vice versa, yielding in total $1 \times 3 + 3 \times 1 = 6$ states. To form a ‘triplet-like’ (+) state in spin-isospin subspace we can combine a spin triplet state with an isospin triplet state or a spin singlet state with an isospin singlet state, giving in total $3 \times 3 + 1 \times 1 = 10$ states.

[†] We note that both the spin and isospin degrees of freedom couple to a magnetic field, and in this work we use the terms “spin” and “isopin” to refer to the spin and isospin magnetic moments (which are the observables in our experiments) opposed to the angular momenta (which strictly speaking cease to be good quantum numbers in the presence of spin-orbit coupling and K-K’ scattering).

To define more specifically these different states we denote the isospin of each electron by K (K') and its spin by \downarrow (\uparrow), where the spin quantization is along the tube axis. One-electron states then read as $|K \uparrow\rangle$, $|K' \uparrow\rangle$, $|K \downarrow\rangle$, and $|K' \downarrow\rangle$, while the non-symmetrized two-electron states read as $|K \uparrow\rangle_1 |K' \uparrow\rangle_2$, $|K' \uparrow\rangle_1 |K' \uparrow\rangle_2$, etc., where the index refers to the first and second electron. After symmetrization or anti-symmetrization the relevant states become, for example:

$$|K \uparrow K' \uparrow\rangle^\pm \equiv \frac{1}{\sqrt{2}} (|K \uparrow\rangle_1 |K' \uparrow\rangle_2 \pm |K' \uparrow\rangle_1 |K \uparrow\rangle_2)$$

In the absence of spin-orbit coupling and electron-electron interactions all the states within the (+) or (-) multiplets are degenerate. However, in the presence of spin-orbit interactions the states split according to the relative alignment of the electrons' spin and isospin. For two electrons there are three different energetic configurations: If both electrons have parallel spin and isospin the energy is $-\Delta_{SO}$, if one has parallel alignment and another antiparallel alignment than the energy is zero, and if both are antiparallel than the energy is Δ_{SO} (where we assumed that the sign of the spin-orbit interactions prefers parallel alignment of spin and isospin) (see Fig. 3 in Ref. 1).

In transport experiments that probe the $1e$ to $2e$ transition, only 7 out of the 16 states are visible due to selection rules imposed by sequential tunneling. Assuming that a single electron initially occupies the ground state $|K \downarrow\rangle$, a second electron can be added to any of the four spin-isospin states if the total wavefunction is spatially anti-symmetric, but can only occupy the other three spin-isospin states if it is spatially symmetric, namely:

$$\begin{array}{l} \text{Spatially} \quad \quad \quad \text{Spatially} \\ \text{Anti-Symmetric} \quad \quad \quad \text{Symmetric} \\ |K \downarrow\rangle + |K \downarrow\rangle \rightarrow |K \downarrow K \downarrow\rangle^- \\ |K \downarrow\rangle + |K' \uparrow\rangle \rightarrow |K \downarrow K' \uparrow\rangle^- \quad \text{or} \quad |K \downarrow K' \uparrow\rangle^+ \\ |K \downarrow\rangle + |K \uparrow\rangle \rightarrow |K \downarrow K \uparrow\rangle^- \quad \text{or} \quad |K \downarrow K \uparrow\rangle^- \\ |K \downarrow\rangle + |K' \downarrow\rangle \rightarrow |K \downarrow K' \downarrow\rangle^- \quad \text{or} \quad |K \downarrow K' \downarrow\rangle^- \end{array}$$

In comparison, transitions such as $|K \downarrow\rangle \rightarrow |K \uparrow K \uparrow\rangle$ are not allowed, as they involve a change in the spin or isospin of both electrons simultaneously. Thus, if transport starts

from one electron in the ground states then there are four anti-symmetric and three symmetric possible end states. The counting is summarized in table S1.

Real Space	Spin \otimes Isospin	Total	Should appear in transport
Symmetric	-	6	3
Anti-Symmetric	+	10	4

Table S1 Counting the two-electron states according to their symmetries in real space.

S2. Direct measurement of the single-particle level spacing

In order to estimate the effect of interactions in our two-electron system, we compare in the main text the splitting between the symmetric and anti-symmetric multiplets, Δ_{S-AS} , with the single-particle level spacing of the right dot, Δ_{1s} . In this section we demonstrate how this level spacing is directly determined from the excitation spectrum of a single electron. We also show that the change in the confining potential of one and two electrons is negligible.

Figure S1a shows the conductance, G , measured as a function of gate voltage, V_g , and source-drain bias, V_{sd} , at the $(0,0) - (0,1)$ transition at $B_{\parallel} = 7$ T. This measurement directly reflects the energy spectrum of a single electron in the right dot. Three pairs of excitation lines, apparent as lines of high conductance, are visible: A low-energy pair (labeled α_1, β_1) a pair at intermediate energies (labeled α_2, β_2) and a pair at high energies, whose splitting is barely visible (labeled γ_1, δ_1). The states $\alpha_1, \beta_1, \gamma_1, \delta_1$ can be directly associated with the four spin-isospin states of the lowest particle-in-a-box level. In fact, their energies perfectly fit the magnetic-field dependence of the states, shown as an orange double-cross in Fig. S1b: The lowest states correspond to $|K \downarrow\rangle$ and $|K \uparrow\rangle$ and their extracted splitting, $E_{\beta_1} - E_{\alpha_1} = 1.4$ meV, matches well the expected splitting: $E_{K\uparrow} - E_{K\downarrow} = \Delta_{SO} + 2\mu_s B = 1.24$ meV (μ_s is the spin contribution to the magnetic moment). States of opposite isospin are split by the magnetic field by $E_{K'} - E_K = 2\mu_{orb} B \approx 15$ meV (μ_{orb} is the orbital contribution to the magnetic moment) matching the observed splitting between the (α_1, β_1) pair and the (γ_1, δ_1) pair. Finally, the high-energy pair of K' states is expected to be split by $E_{K'\uparrow} - E_{K'\downarrow} = 2\mu_s B - \Delta_{SO} = 0.5$ meV,

also faintly observed in the measurement. This clearly demonstrates that the four excitations $\alpha_1, \beta_1, \gamma_1, \delta_1$ are the four spin-isospin states of a single electron in the lowest particle-in-a-box level.

The remaining pair of lines at intermediate energies (α_2, β_2) are separated from the low-energy pair by $E_2 - E_1 = \frac{1}{2}(E_{\alpha_2} + E_{\beta_2}) - \frac{1}{2}(E_{\alpha_1} + E_{\beta_1}) = 7.8 \text{ meV} < 15 \text{ meV}$, and so their isospin must be parallel to the field (K). This pair must then correspond to the first excited level, which for a single electron corresponds to the second particle-in-a-box state. Its corresponding magnetic field dependence is shown in purple in Fig S1b. Specifically we see that the splitting between the states α_2, β_2 , $E_{\beta_2} - E_{\alpha_2} = 1.2 \text{ meV}$ fits well the predicted one $E_{K\uparrow} - E_{K\downarrow} = 1.24 \text{ meV}$.

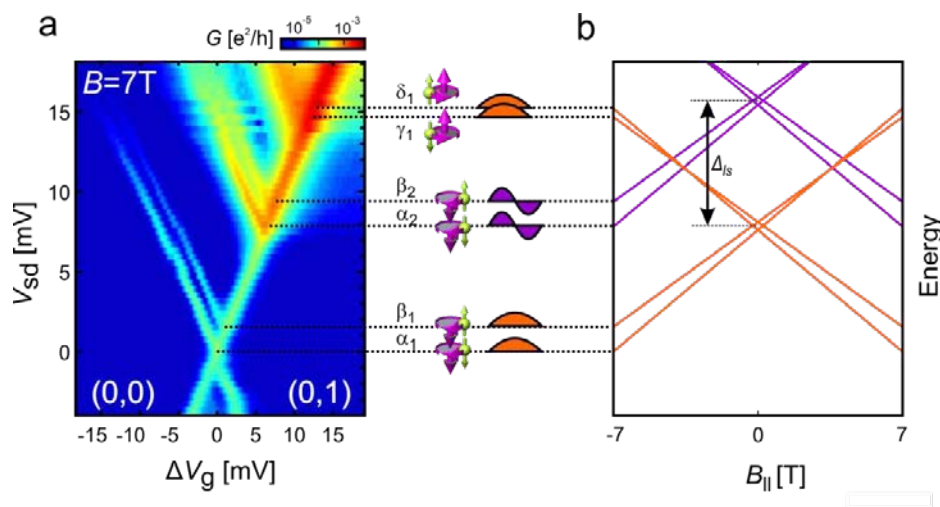


Figure S1: Measurement of the single particle level spacing of the right dot. **a.** One-electron excitation spectrum at the transition (0,0)-(0,1). Conductance G is plotted as a function of gate voltage ΔV_g and source-drain bias V_{sd} at magnetic field $B_{\parallel} = 7 \text{ T}$ featuring parallel lines corresponding to $1e$ excitations. **b.** Predicted magnetic-field dependence of the $1e$ spectrum allowing identification of excitation in **a**. Spin (green) and isospin (magenta) are illustrated by up- and down-pointing arrows. States of the first (second) particle-in-a-box state appear in orange (purple).

Having identified all the states, we can unambiguously determine the single-particle level spacing of the right dot from the energy difference between the (α_2, β_2) and (α_1, β_1) pairs. The level spacing is thus $\Delta_{Is} = 7.8 \text{ meV}$.

In the main text we compare the level spacing, obtained from the measurement of the energy spectrum of a single electron, with Δ_{S-AS} for two electrons. For this comparison to be valid, it is important to verify that the confinement potential shape is not modified

considerably when going from one to two electrons in the dot. This is demonstrated below. Figure S2 presents the conductance, G , measured as a function of gate voltage, V_g , and source-drain bias, V_{sd} , at $B_{\parallel} = 7.5$ T for the first three electrons occupying the right dot (the left remains in the gap). One property of the dot that can change with adding a second electron is its charging energy. By extrapolating the Coulomb blockade diamonds slopes, one extracts a charging energy of $U = 21$ meV for the first electron and $U = 17$ meV for the second electron, a small reduction by only 21%. We note that this reduction is mostly due to a change in the capacitance to the leads, while the capacitance to the gate, which is inversely proportional to the Coulomb diamond width, remains unchanged up to 5%. Since the single-particle level spacing is proportional to the length of the dot, similar to the capacitance to the gate, we conclude that the $1e$ value provides a good estimate.

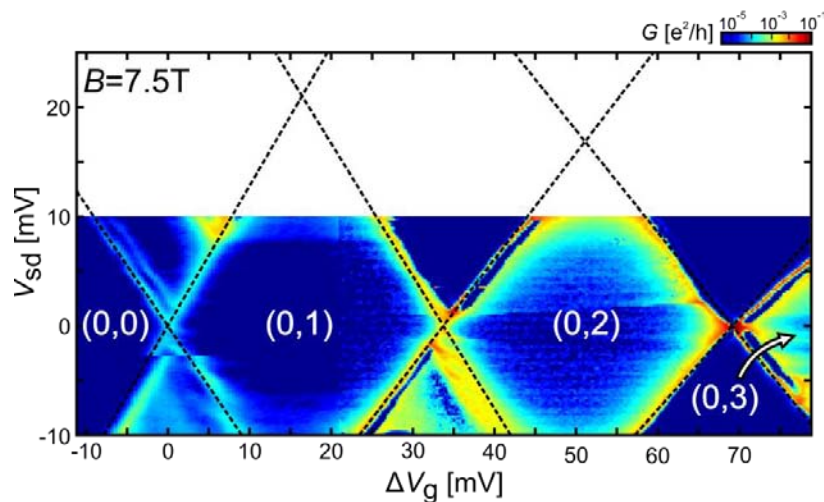


Figure S2: Distortion of the right dot by charging. Conductance G is plotted as a function of gate voltage ΔV_g and source-drain bias V_{sd} at magnetic field $B_{\parallel} = 7.5$ T. The capacitance of the dot to the gate, C_g , related to the horizontal extent of the Coulomb blockade diamonds, ΔV_g , by $C_g = e/\Delta V_g$ is seen to remain constant for one and two electrons. The charging energy, extracted from the vertical extent of the Coulomb blockade diamonds, is reduced by 21% for the second electron.

S3. Comparison of one-electron and two-electron addition spectra.

In the main text we classify the $2e$ states by their symmetry properties according to magnetic-field fingerprints based on the single-particle magnetic properties (Fig. 3). In this section we quantitatively compare the $1e$ spectrum (Fig. S3a) reported before² and

the $2e$ spectrum at the transition to the (1,1) configuration (Fig. S3b, duplicating Fig. 3a in the main text). The two spectra are found to be practically identical, supporting the use of single-particle magnetic properties in the main text.

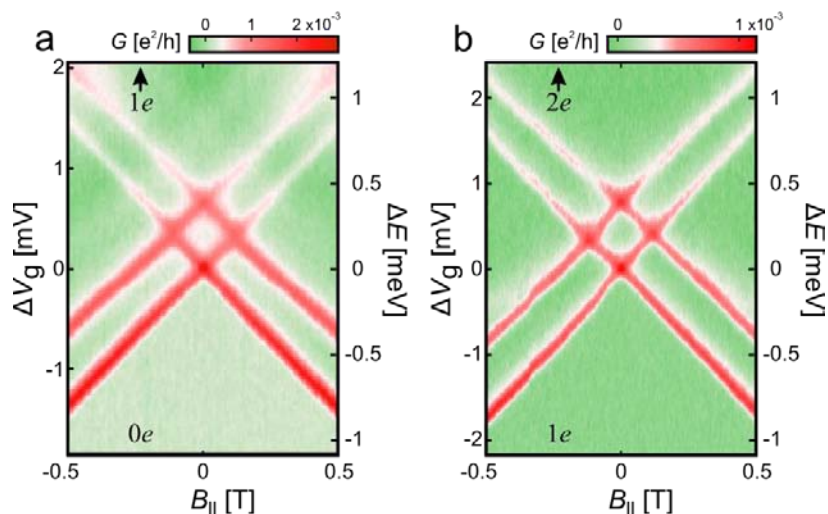


Figure S3: Comparison of one-electron and two-electron addition spectra. **a**, One-electron and **b**, Two-electron magnetic-field dependence of the addition spectrum: G is plotted as a function of ΔV_g and $B_{||}$ at finite bias ($V_{sd} = -2.2$ mV in panel **a**, 2 mV in panel **b**). Lines of enhanced conductance correspond to tunneling via $1e$ (a) and $2e$ (b) states. Panel **b** reproduces Fig. 3a of the main text.

We start by comparing the magnetic moments in the two spectra. From the $2e$ spectrum we extract $\mu = \pm 1.61$ meV/T and $\mu = \pm 1.48$ meV/T for the lower and upper crosses respectively. The average moment corresponds to the orbital contribution to the moment, $\mu_{\text{orb}} = 1.55 \pm 0.01$, whereas the difference corresponds to Zeeman splitting, giving the gyromagnetic factor $g = 2.2 \pm 0.4$, both in good agreement with $1e$ moments reported before ($\mu_{\text{orb}} = 1.55$, $g = 2.1 \pm 0.1$). This allows us to attribute the splitting at $B_{||} = 0$ to spin-orbit coupling, which measures to be $\Delta_{\text{SO}} = 0.36 \pm 0.02$ meV, in excellent agreement with the $1e$ spin-orbit coupling $\Delta_{\text{SO}} = 0.37 \pm 0.02$ meV.

S4. Inter-valley Coulomb interactions in the observed addition spectrum

The measured addition spectra of two electrons (Fig. 3c) or two holes (Fig. S5a) in a single dot, feature two more lines in addition to the seven states described in the main text. In this section we show how interactions, combined with long-lived excited states, may lead to the two extra lines that are not captured by the non-interacting picture. This section starts by describing the effect of inter-valley Coulomb interactions on the

complete two-electron addition spectrum. We then describe how all the lines in the measured spectra can be accounted for by non-equilibrium transport.

We define as inter-valley backscattering (VBS) the Coulomb-interaction process that exchanges the isospins of two interacting electrons (or holes) having opposite isospins. We first note that the effect of VBS is generally small with respect to forward scattering, i.e. Coulomb-interaction processes which do not involve valley exchange, such as inter-valley Hartree-like interactions and all kinds of intra-valley interactions. This allows us to treat VBS within first-order perturbation theory. Forward scattering and quantum confinement then determine the energy splitting between the symmetric and anti-symmetric multiplets, as described in the main text, whereas VBS and spin-orbit interaction determine the splitting within each multiplet, as we describe below. Second, qualitatively speaking, the effect of VBS scattering is short ranged, since it involves large momentum transfer between the scattered particles. It therefore has negligible effect on the spatially anti-symmetric multiplet, where the two electrons have small probability to be one close to the other along the nanotube axis.

By including the effect of VBS in our exact-diagonalization calculation we obtain the $2e$ spatially symmetric spectrum presented in Fig. S4b. The calculation shows two main differences compared to the non-interacting spectrum (Fig. S4a): First, the four-fold degeneracy of the central line at $B_{\parallel} = 0$ is broken by Δ_{VBS} . Second, the apparent spin-orbit gap is enhanced $\Delta_{\text{SO}} \rightarrow \Delta_{\text{SO}}^* = \sqrt{\Delta_{\text{SO}}^2 + \Delta_{\text{VBS}}^2}$. The magnetic fingerprint of the symmetric multiplet is therefore slightly altered by interactions.

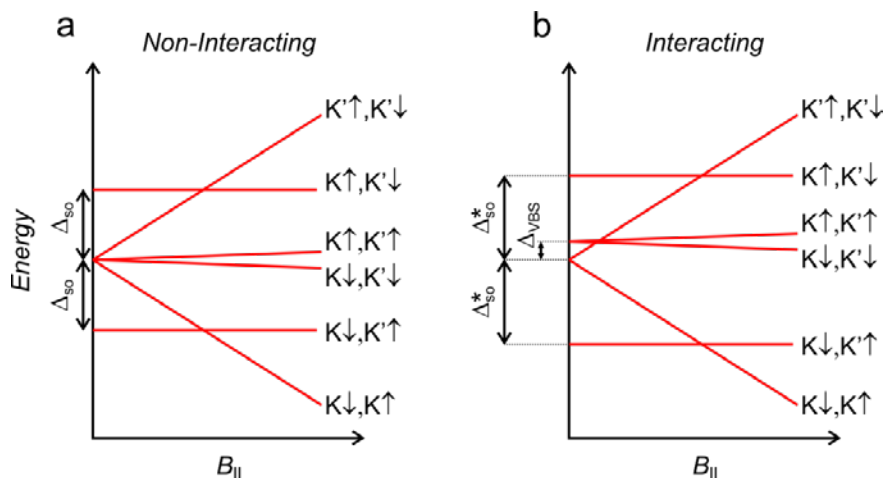


Figure S4 Predicted effect of inter-valley backward scattering on the spatially symmetric $2e$ excitation spectrum. **a.** Schematic energy spectrum of symmetric $2e$ states as a function of B_{\parallel} in the non-interacting picture. The states are split at $B_{\parallel} = 0$ by spin-orbit coupling Δ_{SO} . **b.** same as **a** in the presence of inter-valley backward scattering.

The four-fold degeneracy as $B_{\parallel} = 0$ is lifted by Δ_{VBS} and Δ_{SO} is replaced by $\Delta_{SO}^* = \sqrt{\Delta_{SO}^2 + \Delta_{VBS}^2}$.

Whereas VBS leads to energy shifts in the $2e$ spectrum, interactions alone do not fully account for the measured spectrum. As long as transport starts and ends with a single electron occupying the ground state of the dot, as described in the main text, it leads to 7 spectroscopic lines. However, additional lines would appear if the starting electron occupied instead a *metastable* state having a long lifetime. A natural candidate for such a metastable state is $|K'\uparrow\rangle$, which has spin *and* isospin opposite to the ground state $|K\uparrow\rangle$ leading to long expected relaxation times. Table S2 lists all the processes starting in the $|K'\uparrow\rangle$ state and ending in spatially symmetric $2e$ states, along with their corresponding addition energies in both the non-interacting and interacting cases. The table enumerates three additional $2e$ states that are now accessible, two of which (lines 4-5 in the table) result in extra lines in the spectrum, whereas the last one does not appear in the transport as it lies in the Coulomb-blockaded region (addition energies listed in Table S2 should not be confused with $2e$ energies plotted in Fig. S4).

The measured spectra fully agree with the above picture and from them we extract $\Delta_{VBS} = 0.21 \pm 0.01$ meV for the $2e$ molecule, in agreement with the enhanced $\Delta_{SO}^* = 0.40$ meV, and $\Delta_{VBS} = 0.19 \pm 0.01$ meV for the $2h$ molecule, in agreement with $\Delta_{SO}^* = 0.26$ meV. It is interesting to note, however, that whereas the calculations agree qualitatively with the data and its symmetries, they yield Δ_{VBS} smaller by an order of

magnitude and opposite in sign compared to the value extracted from the experiment. This remaining puzzle is a challenge for future theories trying to understand the finer effects of interactions in this system.

#	Initial 1e state	Final 2e state	Addition energy		Appears in transport?
			Non-Interacting	VBS induced shift	
1	$ K \downarrow\rangle$ (ground state)	$ K \downarrow K' \uparrow\rangle_S$	$E_{K'\uparrow}$	$\Delta_{SO} - \Delta_{SO}^*$	Yes
2		$ K \downarrow K \uparrow\rangle_S$	$E_{K\uparrow}$	0	Yes
3		$ K \downarrow K' \downarrow\rangle_S$	$E_{K'\downarrow}$	Δ_{VBS}	Yes
4	$ K' \uparrow\rangle$ (metastable)	$ K' \uparrow K \uparrow\rangle_S$	$E_{K\uparrow}$	Δ_{VBS}	Yes
5		$ K' \uparrow K' \downarrow\rangle_S$	$E_{K'\downarrow}$	0	Yes
6		$ K' \uparrow K \downarrow\rangle_S$	$E_{K\downarrow}$	$\Delta_{SO} - \Delta_{SO}^*$	No (In blockaded region)

Table S2 Spectroscopic lines of the spatially symmetric multiplet taking into account the metastable state $|K' \uparrow\rangle$ and backward scattering. Lines 1-3 correspond to the three lines discussed in the main text. Lines 4-6 correspond to three additional lines. Lines 1-5 lie within the spectroscopic window and thus appear in transport.

S5. Addition spectrum and detuning dependence of two holes in a single dot.

In the main text we present spectroscopic evidence for the formation of a 2e Wigner-molecule state. In this section we present the detuning dependence and magnetic-field dependence of $2h$ states, both remarkably similar in all aspects to the 2e data. This demonstrates that all the observations presented for electrons in the main paper are in fact generic and do not depend on details such as the charge of the carriers, disorder, and the strength or sign of spin-orbit coupling.

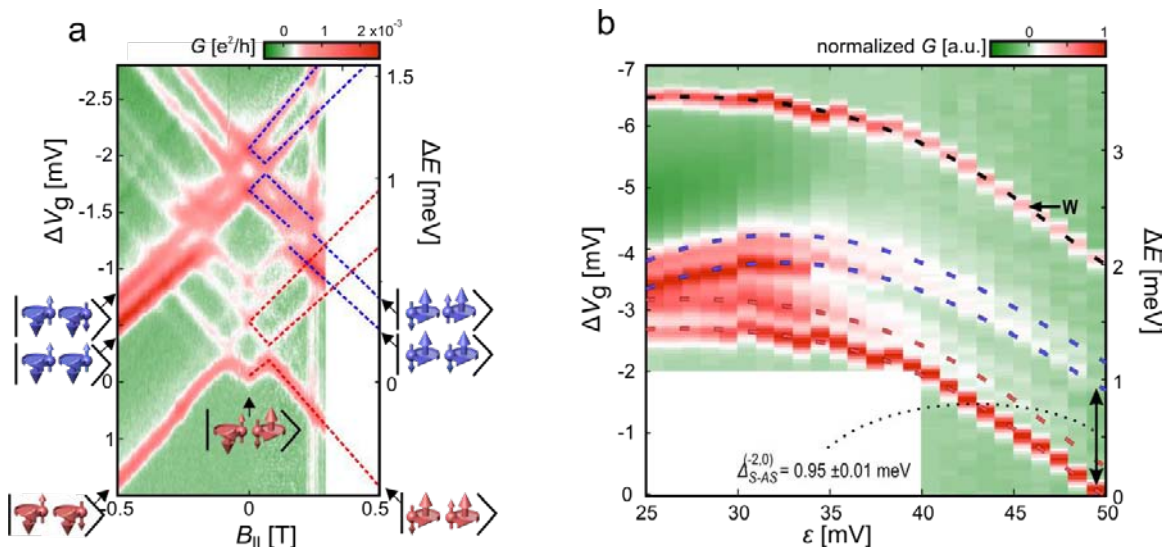


Figure S5: Addition spectrum of a two-hole Wigner molecule. a. Magnetic-field dependent spectrum in the $(2h,0)$ configuration. G is plotted as a function of B_{\parallel} and V_g . ($V_{sd} = -2.5$ mV, $\epsilon = 50$ mV) **b.** Detuning dependence of the spectrum at $B_{\parallel} = 0$ and $V_{sd} = 2$ mV. Dashed lines in **a** and **b** – guides to the eye following the spatially anti-symmetric (blue) and symmetric (red) multiplets and the spectroscopic window (black, W). The inter-multiplet splitting Δ_{S-AS} is extracted from **a**.

Figure S5a presents the magnetic-field dependent $2h$ addition spectrum at the transition $(1h, 0) \rightarrow (2h, 0)$. The conductance measured with $V_{sd} = -2.5$ mV is plotted as a function of B_{\parallel} and V_g (converted to energy on the right y-axis). The lines are matched with the magnetic-field fingerprints: The cusp at $B_{\parallel} = 0$ and the cross above it are identified with the $2h$ symmetric multiplet, whereas the top-most double-cross is identified with the anti-symmetric multiplet. The remaining line is due to inter-valley interactions, as described in section S4 above. The data compares very well to the $1h$ magnetic-field dependence reported before²: The slopes match the $1h$ magnetic moments, and the $B_{\parallel} = 0$ splitting agrees in sign and magnitude with the $1h$ spin-orbit coupling ($\Delta_{SO} = 0.17 \pm 0.02$ meV in the symmetric multiplet and $\Delta_{SO} = 0.20 \pm 0.01$ meV in the anti-symmetric). Finally, the avoided crossing between the $|K \uparrow K \downarrow\rangle$ and $|K \uparrow K' \downarrow\rangle$ states seen in both multiplets at $B_{\parallel} = \pm 0.1$ T matches the $1h$ disorder-induced valley mixing ($\Delta_{KK'} = 0.1$ meV).

Figure S5b presents the detuning-dependent addition spectrum at the $1h-2h$ transition. The conductance is plotted as a function of V_g (converted to energy on the right y-axis) and ϵ at $B_{\parallel} = 0$ and $V_{sd} = 2$ meV. Five lines are seen within the spectroscopic window

(labeled W). From their magnetic-field dependence we identify the two bottom-most lines as the symmetric multiplet and the two top-most lines as the anti-symmetric multiplet, while the remaining line is a result of inter-valley interactions (see S4). Both multiplets undergo a transition from the $(1h,1h)$ charge configuration (up-going slope) to the $(2h,0)$ configuration (down-going slope) as a function of detuning. The $2h$ spectrum presented in Fig. S5a (measured at $\epsilon = 50$ meV) therefore corresponds to two holes in a single dot. Similar to the $(0,2e)$ configuration, the multiplet splitting in the $(2h,0)$ configuration, measured to be $\Delta_{S-AS}^{(2h,0)} = 0.95 \pm 0.01$ meV, is quenched by an order of magnitude with respect to the single-particle level spacing measured in the $(1h,0)$ configuration² $\Delta_{IS}^{(1h,0)} = 11$ meV.

We conclude that the $2h$ system presents quenching of the inter-multiplet splitting, similar to that of the $2e$ system, even though the two systems differ considerably in spin-orbit coupling (holes feature half as strong coupling of opposite sign compared to electrons, favoring anti-parallel spin and isospin compared to parallel in electrons) and in disorder-induced valley mixing (holes feature twice as strong mixing), have opposite charges, and sit in different dots. This supports that the formation of a Wigner-molecule state, manifested by the inter-multiplet excitation energy quenching, is indeed a generic phenomenon which does not depend on the above details of the system.

S6. The complete detuning dependence of excited-state spectra from positive and negative bias measurements.

Due to asymmetric coupling of the dot to the two leads, transport via excited states may appear stronger or weaker depending on the bias direction. In general, transport via excited states that have a strong tunneling barrier to the drain (source) is more visible for positive (negative) bias. Therefore the process $(0,1) \rightarrow (1,1) \rightarrow (0,1)$ is more visible in positive bias (Fig. 1c) while $(0,1) \rightarrow (0,2) \rightarrow (0,1)$ is more visible in negative bias (Fig. 1d). The detuning-dependent spectrum presented in the main text (Fig. S6a, duplicating Fig. 4a in the main text) was measured at negative bias, and its low-detuning excitations are thus very faint. However, the missing lines appear clearly at positive bias (Fig. S6b), and the spectrum is seen to continuously evolve with detuning. This is demonstrated by

plotting the same dashed guidelines on top of the two spectra, taking into account gating effects induced by the opposite source-drain bias.

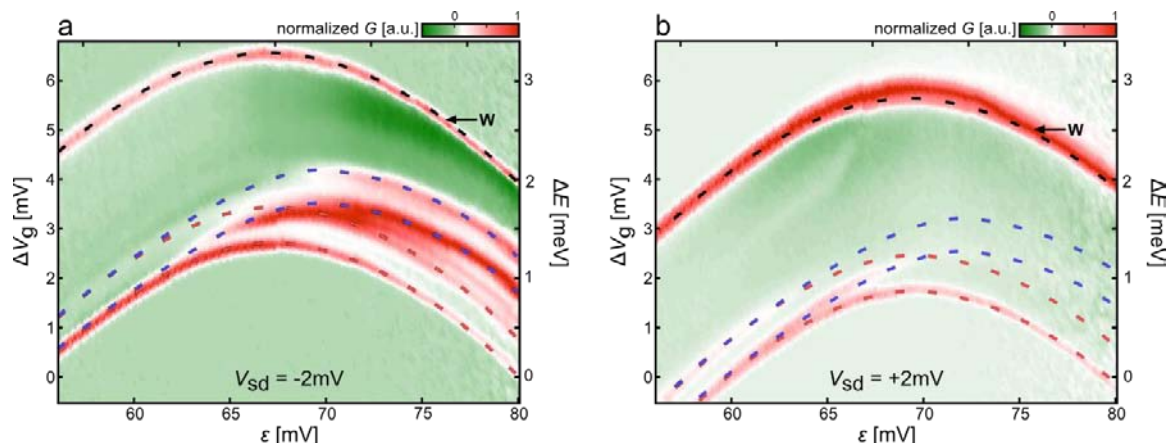


Figure S6: Complete detuning dependence of the $2e$ addition spectrum. **a.** Measurement at negative bias $V_{sd} = -2$ mV (duplicating Fig. 4a in the main text) G is plotted as a function of ϵ and V_g (converted to energy on the right y-axis). **b.** same as **a** with $V_{sd} = +2$ mV showing the low-detuning part of the spectrum that is missing on **a**. Identical guidelines are plotted on top of the two measured spectra, following the symmetric (red) and anti-symmetric (blue) multiplets and the spectroscopic window (black, W). The guidelines are shifted by $\Delta V_g = 1$ mV and $\Delta\epsilon = 2.4$ mV due to gating by the source-drain bias.

S7. Exact diagonalization

In the main text we show the evolution with r_s of two-electron excitation energies in a NT quantum dot (Fig. 4b), together with selected charge-density profiles (Figs. 4c and 4d). These results are obtained by means of the exact-diagonalization method, also known as full configuration interaction. In this section we briefly review the key steps of the calculation. An overview of the method is reported in Ref. 3 and full details on its application to carbon NTs are provided in Ref. 4. With respect to Ref. 4, here we have improved our treatment of VBS interaction.

Since the quantum-dot confinement potential is soft, being induced by electric gates, its generic low-energy dependence on the NT-axis coordinate x is quadratic. Therefore, within the envelope-function and effective-mass approximation, the one-electron wavefunction $\Psi_{n\tau\sigma}(\vec{r}, s)$ may be written as

$$\Psi_{n\tau\sigma}(\vec{r}, s) = AF_n(x)\psi_\tau(\vec{r}) \otimes \chi_\sigma(s) = \varphi_{n\tau}(\vec{r}) \otimes \chi_\sigma(s),$$

where A is a normalization constant, $F_n(x)$ is the envelope-function n th eigenstate of the one-dimensional harmonic oscillator ($n = 0,1,2,\dots$), slowly varying with respect to the graphene lattice constant, $\chi_\sigma(s)$ is the electron spinor (with $\sigma = \pm 1$ being equal to the third component of spin, in units of $\hbar/2$), and $\psi_\tau(\vec{r})$ is the bulk Bloch state whose wave vector is located at the bottom of conduction-band valley τ in reciprocal space (valley K if $\tau = +1$, valley K' if $\tau = -1$, the quantum number τ being the isospin). The one-electron energy $E_{n\tau\sigma}$ is

$$E_{n\tau\sigma} = \hbar\omega_0(n + 1/2) + \Delta_{so}\tau\sigma/2 + \mu_s B\sigma - \mu_{orb}B\tau,$$

where the harmonic-oscillator energy quantum $\hbar\omega_0 = 7.8$ meV is equal to the observed level spacing Δ_{ls} .

Using $\Psi_{n\tau\sigma}(\vec{r}, s)$ as one-electron basis set, the interacting Hamiltonian \hat{H} in second-quantization acquires the form

$$\hat{H} = \hat{H}_{SP} + \hat{V}_{FW} + \hat{V}_{BW}.$$

The single-particle term \hat{H}_{SP} is

$$\hat{H}_{SP} = \sum_{n\tau\sigma} E_{n\tau\sigma} \hat{c}_{n\tau\sigma}^+ \hat{c}_{n\tau\sigma},$$

where the fermionic operator $\hat{c}_{n\tau\sigma}^+$ ($\hat{c}_{n\tau\sigma}$) creates (destroys) an electron with spin σ and isospin τ in the n th level of the harmonic oscillator. The forward-scattering (FS) term

$$\hat{V}_{FS} = \frac{1}{2} \sum_{nn'n''n'''} \sum_{\tau\tau'\sigma\sigma'} V_{nn'n''n'''}^{\tau\tau'\tau'\tau} \hat{c}_{n\tau\sigma}^+ \hat{c}_{n'\tau'\sigma'}^+ \hat{c}_{n''\tau'\sigma'} \hat{c}_{n'''\tau\sigma}$$

includes all intra-valley scattering processes due to Coulomb interaction as well as Hartree-like inter-valley scattering terms. The FS matrix element

$$V_{nn'n''n'''}^{\tau\tau'\tau'\tau} = \iint d\vec{r} d\vec{r}' \varphi_{n\tau}^*(\vec{r}) \varphi_{n'\tau'}^*(\vec{r}') U(\vec{r} - \vec{r}') \varphi_{n''\tau'}(\vec{r}') \varphi_{n'''\tau}(\vec{r})$$

depends on the static dielectric constant κ_r of the electrostatic environment, here treated as a free parameter, through the so-called Ohno potential,

$$U(\vec{r} - \vec{r}') = \frac{e^2}{\sqrt{e^4 / U_0^2 + \kappa_r^2 |\vec{r} - \vec{r}'|^2}},$$

which interpolates the two limits of Coulomb-like long range and Hubbard-like short range interactions (with Hubbard p_z -site parameter $U_0 = 15$ eV). The six-dimensional integral $V_{nn'n''n'''}^{\tau\tau'\tau''\tau''}$ is evaluated by neglecting the overlap of p_z orbitals on different sites and using the slow variation in space of the envelope function $F_n(x)$.

Backward interactions are included in the term

$$\hat{V}_{VBS} = \frac{1}{2} \sum_{nn'n''n'''} \sum_{\tau\sigma\sigma'} V_{nn'n''n'''}^{\tau-\tau'\tau''-\tau''} \hat{c}_{n\tau\sigma}^+ \hat{c}_{n'-\tau\sigma'}^+ \hat{c}_{n''\tau\sigma} \hat{c}_{n'''-\tau\sigma},$$

which exchanges the valleys of two scattering electrons when they have opposite isospins, otherwise it has no effect. The evaluation of VBS matrix elements

$$V_{nn'n''n'''}^{\tau-\tau'\tau''-\tau''} = \iint d\vec{r} d\vec{r}' \varphi_{n\tau}^*(\vec{r}) \varphi_{n'-\tau'}^*(\vec{r}') U(\vec{r} - \vec{r}') \varphi_{n''\tau}(\vec{r}') \varphi_{n'''-\tau''}(\vec{r})$$

lies outside the range of applicability of the standard envelope-function theory. We will show elsewhere that such matrix elements contain the short-range part of interaction, weakly depend on the unknown NT chirality, and are smaller by orders of magnitude than FS matrix elements. On the other hand, FS matrix elements depend only on macroscopic NT parameters such as the radius R , which is deduced by the measured value of μ_{orb} .

We exactly diagonalize the FS Hamiltonian

$$\hat{H}_{SP} + \hat{V}_{FS},$$

which is a matrix in the Fock space of Slater determinants $|\Phi_i\rangle$ that are obtained by filling with two electrons in all possible ways the lowest 50 one-electron orbitals $\varphi_n(\mathbf{r})$ (two-fold spin degenerate at $B = 0$). Both ground and excited two-electron states, $|\Psi_n\rangle$, expanded on the basis of Slater determinants,

$$|\Psi_n\rangle = \sum_i c_i^n |\Phi_i\rangle,$$

are obtained numerically, together with their energies, by means of the parallel home-built code *DonRodrigo*. The diagonalization proceeds in each Hilbert-space sector labeled by the total spin component along the NT axis, total isospin, and parity under mirror reflection with respect to a plane perpendicular to the NT axis, placed in the middle of the quantum dot. The effect of VBS terms on eigenstates $|\Psi_n\rangle$ of FS Hamiltonian is considered at the level of first-order degenerate perturbation theory.

The code output (i.e., the expansion coefficients c_i) is post-processed in order to obtain the charge density $\rho(x)$ for the n th excited state at given r_s ,

$$\rho(x) = \sum_{ij} c_i^n c_j^{n*} \langle \Phi_j | \sum_{mm'\tau\tau'\sigma} F_m^{*}(x) F_{m'}(x) \hat{c}_{m\tau\sigma}^+ \hat{c}_{m'\tau'\sigma} | \Phi_i \rangle.$$

The density parameter r_s is estimated as the ratio of the characteristic harmonic oscillator length to the effective Bohr radius a_B^* ,

$$r_s = \left(\frac{\hbar}{m^* \omega_0} \right)^{1/2} \left(\frac{\hbar^2 \kappa_r}{m^* e^2} \right)^{-1} = \frac{2e^2 (m^*)^{1/2}}{\hbar^{3/2} (\omega_0)^{1/2} \kappa_r},$$

where the electron effective mass m^* is obtained through the formula

$$m^* = \frac{\hbar^2}{3R\gamma},$$

with $\gamma = 0.54$ eV nm being the graphene π -band parameter.

References

1. Von Stecher, J., Wunsch, B., Lukin, M., Demler, E. & Rey, A. M. Double quantum dots in carbon nanotubes. *Physical Review B* **82**, 125437 (2010).
2. Kuemmeth, F., Ilani, S., Ralph, D. C. & McEuen, P. L. Coupling of spin and orbital motion of electrons in carbon nanotubes. *Nature* **452**, 448–452 (2008).
3. Rontani, M., Cavazzoni, C., Bellucci, D. & Goldoni, G. Full configuration interaction approach to the few-electron problem in artificial atoms. *The Journal of Chemical Physics* **124**, 124102 (2006).
4. Secchi, A. & Rontani, M. Wigner molecules in carbon-nanotube quantum dots. *Physical Review B* **82**, 035417 (2010).